Analytica Chimica Acta 1255 (2023) 341120

Contents lists available at ScienceDirect

Analytica Chimica Acta

journal homepage: www.elsevier.com/locate/aca

An enhanced tilted-angle acoustic tweezer for mechanical phenotyping of cancer cells

Hanlin Wang [a], Joe Boardman [a], Xiaoyan Zhang [b], Chao Sun [c], Meng Cai [d], Jun Wei [d], Zhiqiang Dong [e], Mingqian Feng [e], Dongfang Liang [f], Sheng Hu [g], Yu Qian [g], Shuang Dong [g], Yongqing Fu [h], Hamdi Torun [h], Aled Clayton [i], Zhenlin Wu [j], Zhihua Xie [k], Xin Yang [a,*]

[a] Department of Electrical and Electronic Engineering, School of Engineering, Cardiff University, Cardiff, CF24 3AA, UK
[b] International Joint Laboratory of Biomedicine and Engineering, Huazhong Agricultural University and Cardiff University, Wuhan, 430070, PR China
[c] School of Life Sciences, Northwestern Polytechnical University, Xi'an, 710072, PR China
[d] Wuhan iRegene Therapeutics Co., Ltd, Wuhan, 430070, PR China
[e] College of Biomedicine and Health, College of Life Science and Technology, Huazhong Agricultural University, Wuhan, 430070, China
[f] Department of Engineering, University of Cambridge, Cambridge, CB2 1PZ, UK
[g] Department of Thoracic Oncology, Hubei Cancer Hospital, Tongji Medical College, Huazhong University of Science and Technology, Wuhan, 430079, PR China
[h] Engineering and Environment, Northumbria University, Newcastle Upon Tyne, NE1 8ST, UK
[i] Tissue Micro-Environment Group, Division of Cancer & Genetics, School of Medicine, Cardiff University, Cardiff, CF14 4XN, UK
[j] School of Optoelectronic Engineering and Instrumentation Science, Dalian University of Technology, Dalian, 116023, PR China
[k] Department of Civil Engineering, School of Engineering, Cardiff University, Cardiff, CF24 3AA, UK

HIGHLIGHTS

- An acoustic tweezer is developed to distinguish different cell types based on the acoustic contrast factor.
- Reference trajectories combined with new algorithms simplify equipment requirements.
- The acoustic contrast factor and compressibility of cells are measured by cell reference trajectories.
- The acoustic contrast factor and compressibility of different cells show significant differences.

GRAPHICAL ABSTRACT

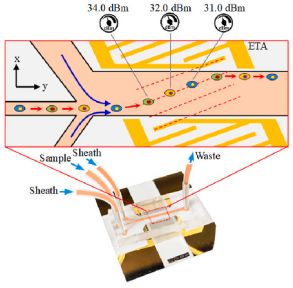

ARTICLE INFO

Handling Editor: Prof Lin Yuehe

Keywords:
Acoustofluidics
Lab on a chip
Acoustic contrast factor
Microfluidics

ABSTRACT

Acoustofluidic devices becomes one of the emerging and versatile tools for many biomedical applications. Most of the previous acoustofluidic devices are used for cells manipulation, and the few devices for cell phenotyping with a limitation in throughput. In this study, an enhanced tilted-angle (ETA) acoustofluidic device is developed and applied for mechanophenotyping of live cells. The ETA Device consists of an interdigital transducer which is positioned along a microfluidic channel. An inclination angle of 5° is introduced between the interdigital transducer and the liquid flow direction. The pressure nodes formed inside the acoustofluidic field in the channel deflect the biological cells from their original course in accordance with their mechanical properties, including volume, compressibility, and density. The threshold power for fully converging the cells to the pressure node is used to calculate the acoustic contrast factor. To demonstrate the ETA device in cell mechanophenotyping, and

* Corresponding author.
E-mail address: yangx26@cardiff.ac.uk (X. Yang).

https://doi.org/10.1016/j.aca.2023.341120
Received 25 October 2022; Received in revised form 1 February 2023; Accepted 17 March 2023
Available online 23 March 2023

distinguishing between different cell types, further experimentation is carried out by using A549 (lung cancer cells), MDB-MA-231 (breast cancer cells), and leukocytes. The resulting acoustic contrast factors for the lung and breast cancer cells are different from that of the leukocytes by 27.9% and 21.5%, respectively. These results suggest this methodology can successfully distinguish and phenotype different cell types based on the acoustic contrast factor.

1. Introduction

Mechanophenotyping is an emerging tool for measuring intracellular content and structure [1]. Characterising cancer cells in combination with mechanophenotyping provides important insights to the heterogeneity of tumour-cell populations in an unbiased and label free fashion. For instance, tumour cells are much stiffer than their healthy counterparts [2], but their intracellular stiffness is reduced resulting in enhancing tumour migration in epithelial-mesenchymal transition (EMT) to promote cancer cells invasion [3]. Mechanophenotyping could also address response to therapies and predict tumour progression and recurrence [4]. Atomic force microscopy (AFM) has been used for assessing the mechanical fingerprints of tumours for early cancer grading/classification, but known to be low-throughput leading to poor sampling efficiency and missed information [5]. Although deformability cytometry overcomes the low-throughput issue, it exposes cells to high strain rates and requires a high-definition and high-framerate camera for capturing cell deformability from image-based evaluation of cell shapes [6].

Acoustofluidic techniques are becoming increasingly important in biological research for separating/aligning bio-particles [7–13], spatial controlling of cells [14], drug delivery [15,16], and drug screening [17]. By delivering acoustic energy into a fluid medium, these devices can non-invasively manipulate bioparticles suspended in the medium through acoustic radiation force and streaming drag force. Tilted-angle standing surface acoustic wave (SSAW) devices have been developed for manipulating biological samples including circulating tumour cells (CTCs) [18], bacteria [19], inflammatory cells [20], and extracellular vesicles [21]. These devices present the pressure nodal lines induced by the SSAW, which are inclined at a specific angle to the flow direction, rather than being parallel to each other. Comparing with prior work using SSAW in bioparticle manipulation, such tilted-angle configuration can achieve higher separation efficiency and sensitivity. The separation efficiency is significantly improved over previous SAW-based cell separators [22]. Apart from separating cells, SAW devices are also applied to characterise cells mainly through tracking their trajectories during the acoustic deflection. These devices have demonstrated their label-free ability in deriving the mechanical properties of the cells such as acoustic impedance [1], acoustic contrast factor [23], and compressibility [23,24]. Compared to flow cytometry, mechanical phenotyping using acoustofluidics appear to be causing less stress on the cells resulting in higher viability after processing. The label-free fashion preserves the sample's original status and outputs acousto-mechanical properties of cells to offer additional biomarkers of various functional or clinically relevant cell states [24].

The acoustic contrast factor of a defined acoustofluidic system reflects the properties of the bioparticle and the medium in terms of density and compressibility [25]. It is an essential parameter to determine the magnitude of the acoustic radiation force and its sign determines whether a bioparticle will move toward the pressure node (PN) or the antinode (AN). For example, using surfactant to modify the sign of the acoustic contrast factor, Zhao et al. has managed to migrate 300-nm particles from the PN to the AN [26]. Owning to the opposite sign of the acoustic contrast factor, SSAW is able to separate lipoproteins from extracellular vesicles without labelling [27]. Other studies utilised the migration trajectory to derive compressibility of living cells, for example, Wu et al. dragged microparticles and cells towards the microfluidic channel sidewall at different segments to calculate the compressibility [24]. The same group also demonstrated the compressibility of three cell types measured by fitting the trajectories [28]. Continuous flow-based acoustofluidic method has characterised various cell types by registering the position when cells leave the acoustic field [23]. Acoustofluidic methods for mechanical phenotyping of cells have demonstrated the advantages in simplicity in the measurement system setup and less dependent on high-profile cameras. By registering the displacement trajectory of the single-cell in the acoustofluidic device, its acoustic contrast factor or other acousto-mechanical properties can be derived.

In this study, an acoustic tweezer based on an enhanced tilted angle (ETA) configuration was developed and applied for mechanophenotyping of live cells. The ETA device enhanced the acoustic pressure by adding additional finger electrodes to the prior work on conventional tilted-angle interdigital transducers (IDTs) [30]. We also developed an algorithm to derive the acousto-mechanical properties including acoustic contrast factor and compressibility of cells. The algorithm greatly reduces the complexity of data processing and the reliance on high-speed image capture device, facilitating the development of real-time mechanical phenotyping of live cells. The acoustic contrast factors of polystyrene (PS) microspheres, with diameters of 5 μm and 15 μm were measured and compared with the nominal values to verify the accuracy of the measurement. Two cancer cell types, A549, MDA-MB-231, and leukocytes were thereafter characterised using the ETA device for measuring their acoustic contrast factor and compressibility. The results demonstrated the successful cell mechanophenotyping, highlighting the versatility of the ETA applications in mechanical phenotyping of cells.

2. Methods

2.1. The device and working mechanism

In this study, the ETA device (Fig. 1a) employs a pair of IDTs which fully cover aside an inclined channel with the inclination angle (θ) of 5°. Compared with the conventional tilted-angle IDT, the ETA IDTs are patterned with additional and extended finger electrodes to cover the area immediately adjacent to the channel. The ETA device with the same footprint as the conventional IDTs can reduce the working area (ETA: 40 mm^2, conventional IDT: 70 mm^2) to increase the acoustic pressure (~32%) inside the microfluidic channel, which is essential to effectively attract cells to the PNs on their arrivals to the acoustic region. The ETA structure is applied in mechanical phenotyping of cells for the first time.

The ETA device has the common advantage of tilted angle-based IDT, e.g., generating multiple PN lines in the acoustic region inclined to the channel, which increases the length the cells being migrated by the acoustic field. The ETA configuration further improves the efficiency by producing a stronger acoustic pressure to generate a higher acoustic radiation force ($\boldsymbol{F}_r$) on microparticles in the acoustofluidic field. The approximation of cells in suspension culture as microsphere is made by other works [28–30]. Thus, driven by the $\boldsymbol{F}_r$, the cell migration trajectory is determined by both the mechanical properties of the cells (size, density, and compressibility) and the condition of the acoustofluidic environment. Of which, the input power (P_1) determines the degree of acoustic pressure (P_0) and in turn, the scale of the $\boldsymbol{F}_r$ [31],

$$P_0 = \sqrt{\frac{\alpha P_1 \rho_s C_s}{A_w}}, \tag{1}$$

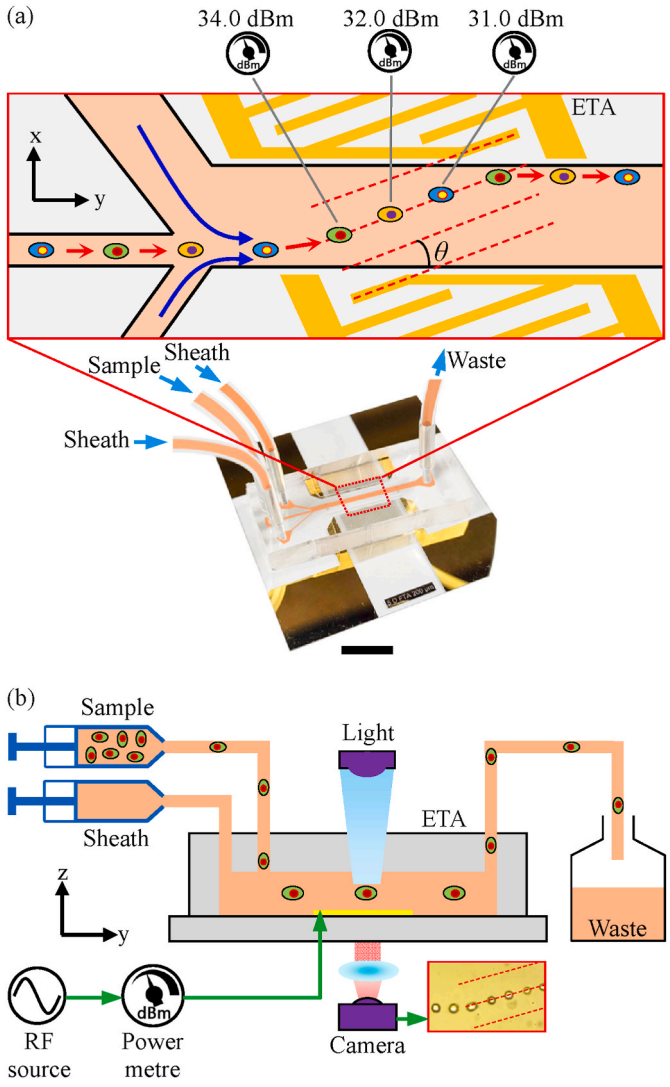

Fig. 1. An enhanced titled angle (ETA) acoustofluidic device for mechanical phenotyping of cells. (a) Working mechanism of the ETA-based cell mechano-phenotyping. The input power for effectively trapping cell to the PN is associated with the cell's mechanical properties. Cells are convergent to the first nearest PN driven by the acoustic radiation force ($\boldsymbol{F}_r$). The scale bar is 1 cm. (b) The diagram of the system setup. The power metre is used for registering the minimum input power for trapping the cells to the first nearest PN.

$$\boldsymbol{F}_r = -\left(\frac{\pi P_0^2 V_P \beta_m}{2\lambda}\right)\varphi \sin(2kx), \tag{2}$$

$$\varphi = \frac{5\rho_P - 2\rho_m}{2\rho_P + \rho_m} - \frac{\beta_P}{\beta_m}, \tag{3}$$

where P_0, λ, V_P, β_m, β_p, φ, k, x, α, P_1, ρ_s, ρ_p, ρ_m, C_s and A_w are acoustic pressure amplitude, SAW wavelength, cell volume, compressibility of medium, cell compressibility, acoustic contrast factor, acoustic wavenumber, distance from a pressure node, power conversion efficiency, RF input power, the density of the substrate, cell density, the density of the medium, surface wave phase velocity, and acoustic working area, respectively.

When a cell maintains a constant velocity in the acoustic field, the acoustic radiation force and streaming drag force ($\boldsymbol{F}_d$) balance each another [32],

$$\boldsymbol{F}_r + \boldsymbol{F}_d = 0, \tag{4}$$

$$\boldsymbol{F}_d = -6\pi\mu R_P(u - u_f), \tag{5}$$

where μ, R_P, u, u_f are viscosity of the medium, cell radius, cell velocity, flow velocity, respectively.

By tuning the input power, we managed to control different cells to follow a similar trajectory converging to the PN line (Fig. 1a). The benefit of using only the input power as the input variable to determine the mechanical properties of cells is the simplicity of reading power values from power meters. This can eliminate the use of a high-profile camera to capture the migration path and simplify the calculation of the acoustic contrast factor and compressibility. By solving Eqns (1)–(5), the velocity of the cell in the ETA device can be expressed by,

$$u = A\varphi \sin(2kx) + u_f, \tag{6}$$

$$A = \alpha\frac{\pi R_P^2 \beta_m P_1 \rho_s c_s}{9A_w\lambda\mu}, \tag{7}$$

where A is considered as the velocity amplitude induced by the acoustic radiation force. The α is calibrated to be 0.1 using the method described in Li's work [10].

Considering the cells' movement time (T) in the channel, the displacement (S) of the cell can be described by integrating the velocity over time,

$$\boldsymbol{S}\int_0^T u\mathrm{d}t = \int_0^T A\varphi \sin(2kx) + u_f\mathrm{d}t. \tag{8}$$

Given the inclined angle of θ between the IDTs alignment and the channel centerline as shown in Fig. 1a, Eqn (8) can be transformed into,

$$\boldsymbol{s}_x = \int_0^T \left[-A\varphi \sin(2kx)\sin\theta + u_f\right]\mathrm{d}t, \tag{9}$$

$$\boldsymbol{s}_y = \int_0^T A\varphi \sin(2kx)\cos\theta\mathrm{d}t \tag{10}$$

where $\boldsymbol{s}_x$ is the transverse component of the displacement in the channel and $\boldsymbol{s}_y$ is the longitudinal component of the displacement. For the channel of a rectangular cross-section with the width w and height h, the flow velocity can then be given by the following equation [33],

$$u_f = \frac{4h^2\Delta P}{\pi^3\mu L}\sum_{n,\mathrm{odd}}^{\infty}\frac{1}{n^3}\left[1 - \frac{\cosh(n\pi\frac{x}{h})}{\cosh(n\pi\frac{w}{2h})}\right], \tag{11}$$

where ΔP is the pressure difference over the channel length L. Assuming a fixed wavenumber k and a fixed flow velocity u_f, the product of A and φ indicates the influence of $\boldsymbol{F}_r$ on the cell trajectory. Under the conditions that the device and fluid conditions are unchanged, the product of A and φ shall be the same for any cells following the same trajectory, regardless of the cell mechanical properties. To obtain the product of A and φ under the same device and fluid conditions, a reference microparticle with its known mechanical properties is firstly introduced into the microchannel. The input power is recorded and the reference trajectory of the microparticle motion is precisely tracked. The product of A and φ for this experiment can be calculated, which is recorded as reference product, $A_1\varphi_1$. For any unknown particle, by adjusting the input power P_1 to converge it to the reference trajectory, one can determine the A of the unknown particle by using Eqn (7), and then the acoustic contrast factor φ of the unknown particle,

$$\varphi = \frac{A_1\varphi_1}{A}. \tag{12}$$

$$\varphi = \frac{9A_1\varphi_1\lambda\mu A_w}{\pi R_P^2\alpha P_1\rho_s C_s\beta_m} \tag{13}$$

Therefore, the acoustic contrast factor of any cell/fluid combination

can be calculated once the cell radius and the device input power are known. Finally, transferring Eqn (3) to determine the compressibility of cells by substituting the acoustic contrast factor value to

$$\beta_P = \left(\frac{5\rho_p - 2\rho_m}{2\rho_P + \rho_m} - \varphi\right)\beta_m. \quad (14)$$

2.2. Numerical simulation

Numerical simulations were performed to reveal the trajectories of particles on the x-z and x-y planes, respectively. The cross-sectional acoustic pressure distribution and particle trajectory were solved using the finite element software package COMSOL Multiphysics. The module "Thermoviscous Acoustics" was used to numerically compute the acoustic pressure distribution in the frequency domain. The trajectories of particles were simulated using the "Particle Tracing model". The system was simplified by the two-dimensional cross-sectional modelling in a rectangular domain with a width of 800 μm and a height of 60 μm [34]. The polydimethylsiloxane (PDMS) wall of the channel was modelled by impedance boundary condition, and the piezoelectric substrate was modelled by applying a displacement function at the domain bottom. The projections of the particles' trajectories on the x-y plane were predicted by integrating Eqn (4) with respect to time in MATLAB, with a given position when a particle initially enters the microchannel. In the x-z plane simulation, we studied three different sizes of polystyrene (PS) microsphere: 5 μm, 10 μm, and 15 μm. The input power applied to the IDTs varies in the range from 20 dBm to 34 dBm, with an incremental step of 0.5 dBm.

2.3. Fabrication and system setup

Fig. 1a show a photo of the ETA device used in the present work. The device is consisted of a PDMS channel and ETA IDTs patterned on a 128° Y-cut X-propagation $LiNbO_3$ piezoelectric substrate. The IDTs were deposited onto the $LiNbO_3$ substrate using a photolithography technique followed by a lift-off process. The IDTs were patterned with 52 pairs of finger electrodes, which have identical finger width and spacing of 50 μm resulting in a high quality factor of the IDT ($Q \approx 26$). The aperture size is 10 mm to accommodate the channel length (more dimensions are provided in Fig. S1, SI). The working frequency was measured by using a vector network analyser (E5061B ENA, Keysight). The measured value of ~19.632 MHz is close to the theoretical value of 19.985 MHz determined by $= \frac{c}{\lambda}$, where c is the speed of sound in $LiNbO_3$ (3997 ms^{-1}), λ is the SAW wavelength (200 μm). The minor difference between the measured and theoretical values could be caused by the capacitance/inductance introduced by the busbars connected with the IDTs.

The PDMS channel had a central inlet for sample flow, and two sheath flow inlets to hydrodynamically focus the cells before entering the acoustic field. The channel was fabricated using standard photolithography and PDMS casting techniques. The length, width, and height of the channel in the acoustic region were 1 cm, 800 μm, and 60 μm, respectively. The PDMS channel and the $LiNbO_3$ substrate were aligned under an inverted microscope and bonded after treated with oxygen plasma (HPT-100, Henniker Plasma). The device was sat on the inverted microscope with a camera to record the trajectory of the cells/microparticles (Fig. 1b). Three inlets were connected to three plastic syringes which were driven by three syringe pumps (WZ-74905, Cole-Parmer) separately. The ETA IDT was electrically connected to a signal generator (N5166B CXG, Keysight Technologies) through a power amplifier (100A250A, Amplifier Research) and a coupler (86207A, Keysight Technologies). The forward and reflected powers were measured using two power meters (U2004A, Keysight Technologies). Before introduction of microparticles or cells, ethanol was used to flush the PDMS channel to remove air bubbles. Then, 2.5% bovine serum albumin (BSA) was used to coat the channel walls to avoid bioparticles attachment. The flow rates of the two sheaths were 5 μl/min and 4 μl/min, respectively, while the sample flow rate was 0.2 μl/min.

Before measuring cancer cells and leukocytes, PS microspheres were used to establish the reference trajectory and validate the accuracy of measuring the acoustic contrast factor. Firstly, 10 μm PS (72986, Sigma-Aldrich) microspheres were chosen to generate the reference trajectory by tuning the input power from 20 dBm to 30 dBm. Then, the acoustic contrast factors of 5 μm (79633, Sigma-Aldrich) and 15 μm PS microsphere (74964, Sigma-Aldrich) were obtained individually to benchmark with the nominal value.

To test the feasibility of using the acoustic contrast factor to mechanophenotype cells, adenocarcinoma human alveolar basal epithelial cells (A549), triple-negative breast cancer cells (MDA-MB-231), and leukocytes were tested separately in the ETA device. The entering position of the field of view of the microscope was located at the beginning of the acoustic zone, where the cells started to deflect. To determine the threshold input power, the lateral displacement of the cell was recorded while turning up the input power until most of the cells are converged to the PN line. Considering there was a deviation (similar with the particle deviation in simulation results shown in Fig. 3a) before cells were converged to the PN line, the cells that displaced over 80% of the maximum lateral displacement (~271 μm) were regarded to be convergent to the PN line, as shown in Fig. 2a.

2.4. Cell preparation and data analysis

In this study, we used commercially sourced A549 (CCL-185, ATCC) and MDA-MB-231 (HTB-26, ATCC) cells. Leukocytes were separated from the whole blood donated by healthy volunteers using EDTA tubes (367835, BD). This study had been granted the approval from Huazhong Agricultural University's Ethics Committee prior to blood sampling. The whole blood was firstly incubated with lysis buffer for 12 min to remove the erythrocytes. Next, leukocytes were collected by centrifuging the blood solution at 1300 rpm for 5 min at room temperature. Two fluorescent dyes, Hoechst 33342 (62249, Thermo Fisher Scientific) and propidium iodide (P1304MP, Thermo Fisher Scientific), were used for staining the cells. This fluorescent labelling approach was simply to allow tracking of cell trajectories in the device, by using the fluorescence microscope. After staining, the leukocyte, A549, and MDA-MB-231 pellets were resuspended individually in a liquid mixture of glycerol and 1 × PBS (volume ratio 1:4). The sample concentration of the three types of cells were close to 2×10^5 cells/mL. Cell samples were photographed under the microscope, and the 2D cell area was measured using ImageJ software. Since the cells were considered to be spheres in suspension culture, they were assumed to be spherical in the numerical simulation and following analysis.

All experiments were performed at least three times, and the results were reported as means ± standard deviations using one-way ANOVA analysis. In addition, every two groups of cells were directly subjected to a T-test to obtain the statistical difference.

3. Results and discussion

3.1. Simulation and reference trajectory

Fig. 2b shows the acoustic pressure inside the channel along the y-axis near the entry and exit points of the acoustic region. On the x-z plane, stable PNs and ANs are generated and orderly arranged along the x-axis with an equal shift of the PNs and ANs due to the inclination angle between the IDT and the channel. The microparticles enter the SAW region which consists of a series of ANs (blue area in the simulation) and PNs (red area in the simulation). One can adjust the acoustic pressure intensity by varying the RF input power (represented by the intensity of acoustic pressure) to drive two types of cells, e.g., leukocytes and cancer cells, to converge to the PN following a similar trajectory, as shown in Fig. 2c. The converging trajectory can be achieved by tuning only the RF input power disregarding the properties of these microparticles

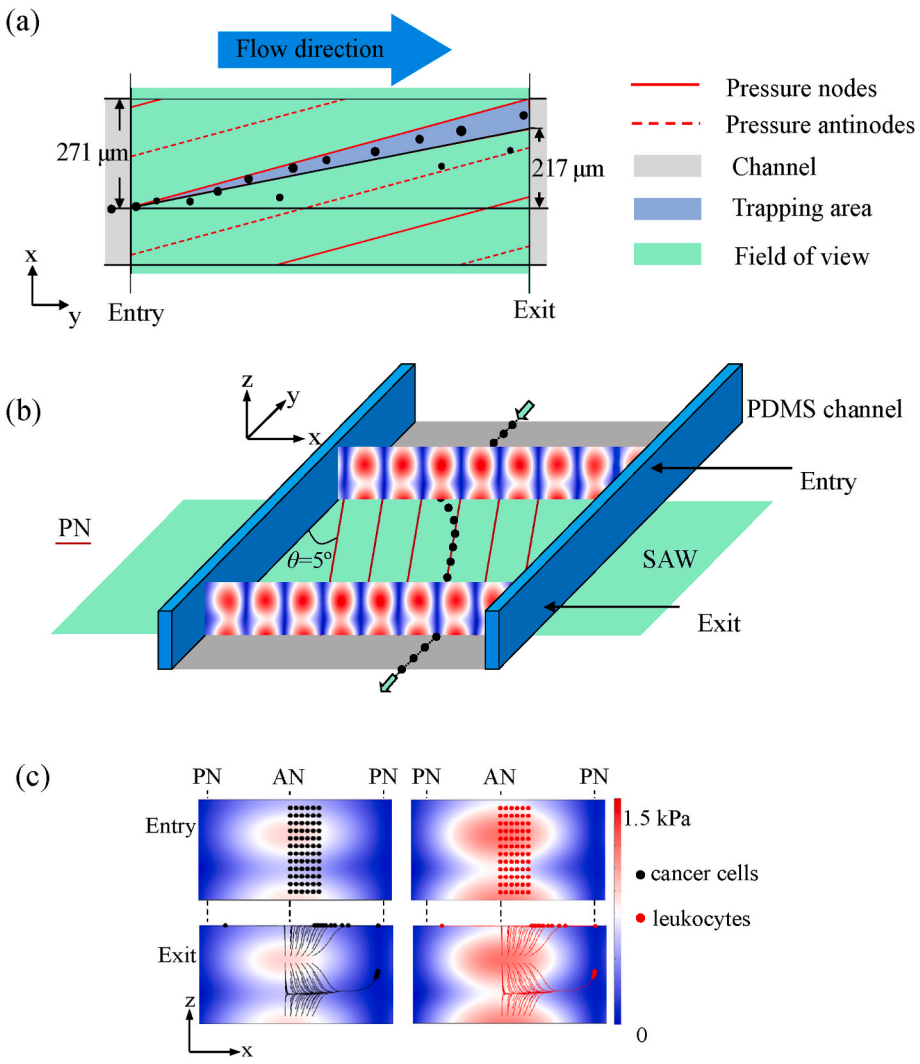

Fig. 2. Simulation of the ETA device for mechanical phenotyping. (a) Under the threshold input power, 80% of cells are convergent to the lateral position (x-axis) between 217 μm and 270 μm when leaving the field of view. (b) Acoustic pressure distribution at the entry and exist (colours indicate the magnitude of acoustic pressure, from 0 kPa (blue) to 1.5 kPa (red)). (c) Two cell types (leukocytes and cancer cells) follow the same converging trajectory under different input powers, represented by acoustic pressures. (For interpretation of the references to colour in this figure legend, the reader is referred to the Web version of this article.)

(volume, compressibility, and density). One can achieve the same time for converging leukocytes and cancer cells to the PNs under acoustic pressures of 1.2 kPa and 0.7 kPa, respectively. The COMSOL simulation results prove the feasibility of adjusting the acoustic pressure (determined by the RF input power) to enable the convergence of various cells to the PNs.

On the x-y plane, the lateral movements of given microparticles, e.g., 10 μm PS microspheres, under different input powers ranging from 26.5 dBm to 29.5 dBm is illustrated in Fig. 3a. There exists a threshold input power, i.e., 28.5 dBm, which drives 10 μm PS microspheres to quickly converge to the nearest PN line (solid grey lines) and shift upwards along the PN line. We investigated various particle parameters and found the same trend where particles would be convergent to the first nearest PN line soon after entering the acoustic region when the RF input power was higher than the threshold, while the particle would escape from the first nearest PN line when the input power was smaller than this threshold, such as 28 dBm in Fig. 3a. The calculated trajectories of 5 μm and 15 μm PS under various input powers are provided in the SI.

For the ease of observation and judgement, we defined the trajectory, which firstly became convergent to the first nearest PN line, as the reference trajectory. Considering that the microparticle followed a wavy path before being convergent to the PN line, the threshold input power was determined when 75% of microparticles were convergent to the PN. In this study, we used the trajectory of 10 μm PS microspheres under 28.5 dBm as the reference trajectory, and the reference product $A_1\varphi_1$ is 0.0018. The experimental reference trajectory is shown in Fig. 3c, in which the 10 μm PS microspheres well follow the theoretical trajectory (blue band) defined by Eqn (6). As described in the previous section, the same trajectory corresponds to the same product of A and φ. Therefore, the acoustic contrast factor of any unknown microparticle/cells can be solved by substituting their threshold input power and size observed in the experiment.

3.2. Acoustic contrast factor measurement of microspheres

To validate the accuracy of using this method to calculate the acoustic contrast factor, PS microspheres of 5 μm and 15 μm were tested. The trajectories of the 5 μm and 15 μm PS microspheres converge to the PN soon after entering the acoustic region, at 34.5 dBm and 25.0 dBm, respectively, as shown in Fig. 3(b) & (d). This agrees with the results we predicted by Eqn (13), where the difference in radius caused a difference of 6 dB and −3.5 dB for the threshold input power, respectively (The threshold input power is inversely proportional to the square of the radius for the same material parameters of microspheres). The red and green bands in Fig. 3(b) & (d) are the numerical simulation trajectories for the 5 μm and 15 μm microspheres, respectively. According to Eqn (13), the measured acoustic contrast factor for 5 μm and 15 μm PS microspheres are 0.1985 and 0.1966, respectively, which are very close to the derived value of 0.1939 [22]. The slight difference of 2.37% and 1.39% may be due to the size deviation of PS microspheres as noted by

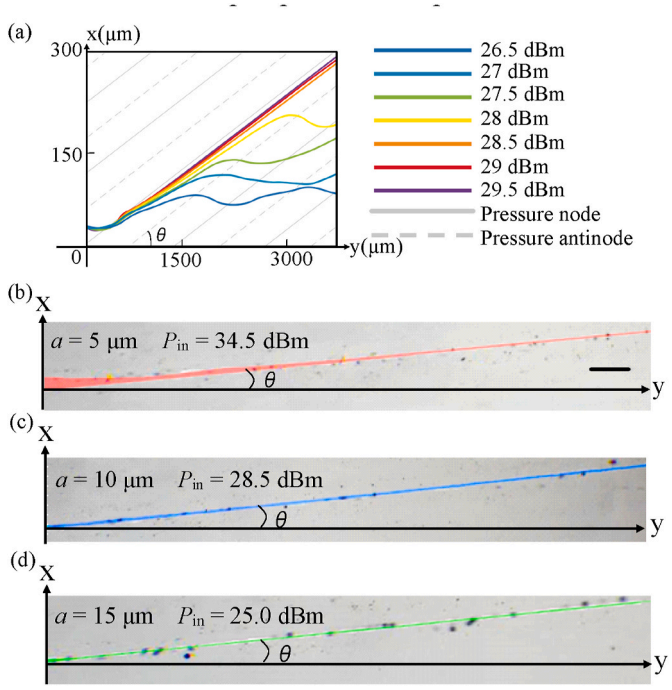

Fig. 3. Numerical and experimental trajectories of the polystyrene (PS) microspheres in the ETA device. (a) Plot of numerical trajectories for 10 μm PS microspheres with increment of the input power. Convergence to the first nearest PN line presents once the threshold input power is met. (b)–(d) Optical images show the experimental trajectories of 5 μm, 10 μm, and 15 μm PS microspheres converging to the first nearest PN line. The red, bule, and green bands are simulation trajectories under the respective input power. (Scale bar, 200 μm). (For interpretation of the references to colour in this figure legend, the reader is referred to the Web version of this article.)

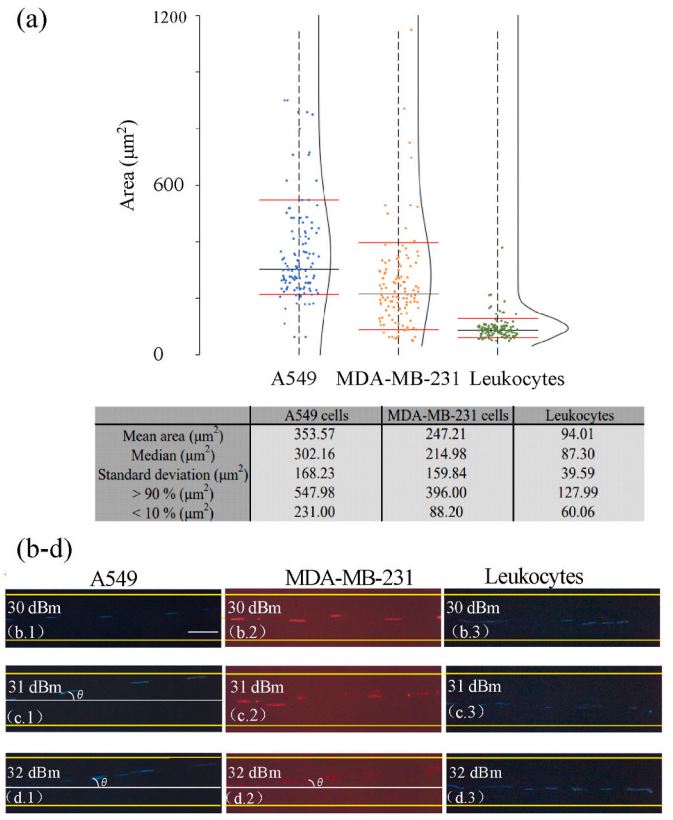

	A549 cells	MDA-MB-231 cells	Leukocytes
Mean area (μm²)	353.57	247.21	94.01
Median (μm²)	302.16	214.98	87.30
Standard deviation (μm²)	168.23	159.84	39.59
> 90 % (μm²)	547.98	396.00	127.99
< 10 % (μm²)	231.00	88.20	60.06

Fig. 4. Size distribution and experimental trajectories of A549, MDA-MB-231, and leukocytes. (a) Size distribution of the three cell types. Red horizontal lines show the 10th and 90th percentiles, black horizontal lines show the median value, black curves show the distribution (n = 120). The table show the area measurement results of the A549, MDA-MB-231 cells, and leukocytes. (b)–(d) Fluorescence imaging of the three cell types translating through the channel under the input power of 30 dBm, 31 dBm, and 32 dBm. (Scale bars, 500 μm) The images show that two cancer cells finally converge to the PN line in which 'θ' is annotated. Leukocytes remain close to their original course without notable deflection towards the PN line. (For interpretation of the references to colour in this figure legend, the reader is referred to the Web version of this article.)

the datasheet (5 ± 0.1 μm and 15 ± 0.2 μm). This result confirms the good accuracy of the proposed method for mechanophenotyping. The small random dots in the three images (Fig. 3b–d) are the dust/microspheres adhered to the channel surface.

3.3. Measurement of cell area and threshold input power

As shown in Fig. 4a, the A549 cells are generally larger than the MDA-MB-231 cells, and both types of cancer cells are considerably larger than leukocytes with the mean area of 353.57 μm^2, 247.21 μm^2, and 94.01 μm^2, respectively. The size distribution of the leukocyte is narrower than that of both the A549 and MDA-B-231 cells, which well agrees with the high heterogeneity of cancer cells in their size [35]. The difference between 90 percentage and 10 percentage lines of leukocytes is only 67.93 μm^2, while that of the two cancer cell groups are 316.98 μm^2 for the A549 cells and 307.8 μm^2 for the MDA-MB-231 cells.

As the input power increases, cell deflection from the original course is shown in Fig. 4b–d. Once the threshold input power is applied, the cells are converged to the PN line with an inclination angle of $\theta = 5°$ to the channel wall. The A549 cells start to deflect under the input power of 30 dBm (Fig. 4b1) whereas the MDA-MB-231 and leukocytes almost remain on their original paths (Fig. 4b2 & 4b3). Increasing the input power to 31 dBm enables the A549 to converge to the PN line (Fig. 4c1), the same power also slightly deflects the MDA-MB-231 (Fig. 4c2) towards the PN line. The leukocytes keep the baseline trajectory with the input power up to 32 dBm (Fig. 4b3, 4c3 & 4d3), which indicates that a higher threshold input power is required for leukocytes to converge to the PN line. Both the MDA-MB-231 and A549 cells acquire sufficient momentum and are finally converged to the PN line under 32 dBm (Fig. 4d1 & 4d2). The heterogeneity of cancer cells results in intercellular variability in deflection but the wavy trajectories towards the PN line as denoted in Fig. 4c2 are in line with the simulation when the input power is below the threshold power (Fig. 3a).

Since the mechanical property of any same type of cells is not uniform, the movement of cells is not identical and thus does not manifest as a single line of trace during the experimental process. Our results reveal that there exists the trajectory of a cell subset convergent to the PN line at low input powers, while another cell subset shows less or no visible deflection under the same conditions. In order to more accurately assess whether the cell deflection approximates to the reference trajectory, we recorded the changes in x coordinate that occurred as the cell entered and exited the field of view and then calculated the lateral displacements. With the increase of the RF input power, the lateral displacement of the three different cells gradually converged to around 271 μm (Details of the observation can be found in the SI). For A549 cells as shown in Fig. 5a, as the input power is increased from 29 dBm to 31 dBm, the 75th percentiles (red bars in the figure) are fixed at around 270 μm, and the 25th percentiles increase from 97.5 μm to 237.5 μm. For MDA-MB-231 cells (Fig. 5b), the 75th percentiles gradually increase from 250 μm to 320 μm and the 25th percentiles increase from 70 μm to 260 μm as the input power increase from 30 dBm to 32 dBm. A similar trend is observed for leukocytes (Fig. 5c), as the input power increase from 32 dBm to 34 dBm. Finally, the cell traces comply with the reference trajectory with the input powers of 31 dBm, 32 dBm, and 34 dBm

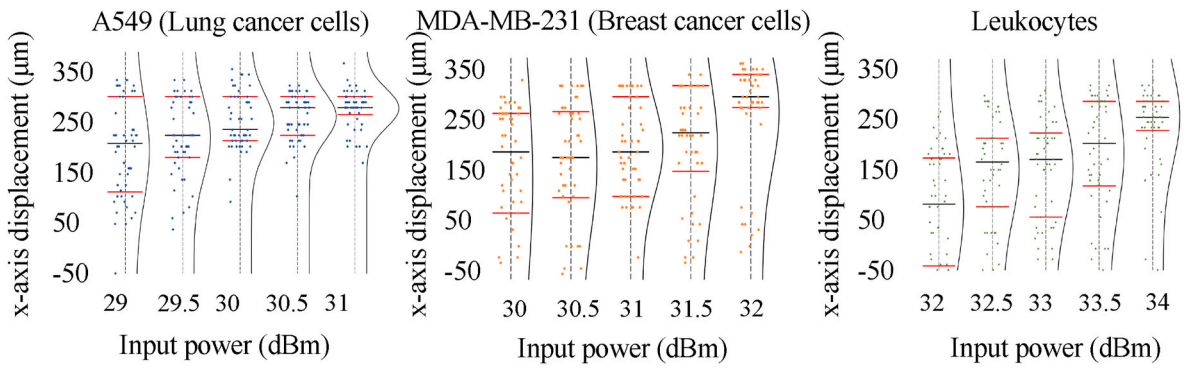

Fig. 5. Distribution plots of cells under different input powers. (a) A549, (b) MDA-MB-231, and (c) leukocytes show convergence to the PN line under 31 dBm, 32 dBm, and 34 dBm, respectively. Top and bottom red horizontal bars show the 25th and 75th percentiles, respectively. Black horizontal bars show the median value, black curves show the distribution (n = 150). (For interpretation of the references to colour in this figure legend, the reader is referred to the Web version of this article.)

for A549, MDA-MB-231 and leukocytes, respectively, which are defined as the threshold input powers of the three types of cells. The reason exceeded the maximum theoretical lateral displacement is probably because the cells are also subject to focusing on the z direction (Fig. 2d), which may cause some of the cells to attach to the channel top wall and change the local acoustofluidic field.

3.4. Calculation of the acoustic contrast factor and the compressibility

After obtaining the deflection threshold of input powers and cell areas, the acoustic contrast factors of three types of cells were calculated using Eqn (11), and their compressibility were calculated by assuming the density of the cells (leukocytes: 1,019 ±3 k · gm^{-3}, tumour cells: 1,051 ±3 k · gm^{-3}) [22,24,36]. As shown in Fig. 6a, leukocytes have the greatest acoustic contrast of 0.147, which may be the result of their smaller compressibility and relatively smaller density. The acoustic contrast factors of A549 cells and MDA-MB-231 cells are 0.106 and 0.115. The difference in the acoustic contrast factors between cancer cells (A549 and MDA-MB-231) and leukocytes are found to be 27.9% and 21.5%, respectively. However, the corresponding difference in compressibility of these two groups is 8.0% and 6.7%, respectively, as shown in Fig. 6b, where the compressibility of the three cell types is 4.35 ± 0.01 × 10^{-10} Pa^{-1} (A549), 4.30 ± 0.01 × 10^{-10} Pa^{-1}(MDA-MB-231), and 4.02 ± 0.01 × 10^{-10} Pa^{-1} (leukocytes).

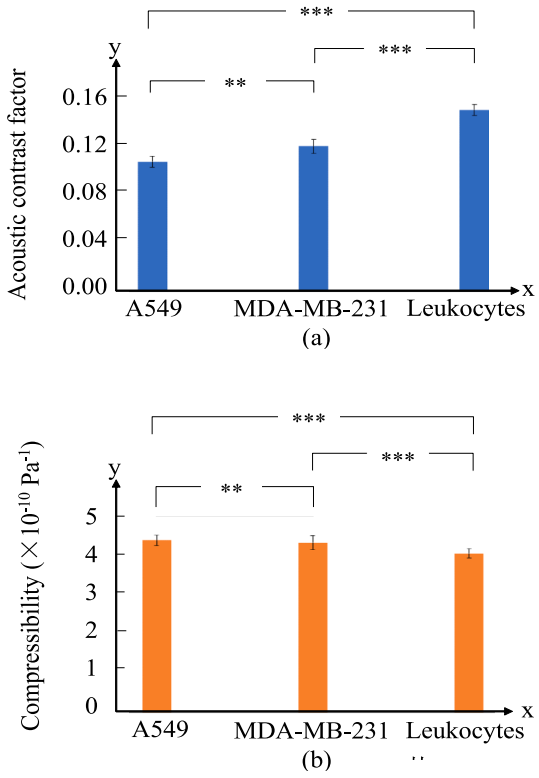

Fig. 6. The acoustic contrast factor (a) and compressibility (b) of A549, MDA-MB-231, and leukocytes. *** and ** indicate p < 0.001 and p < 0.01, respectively.

The difference in the acoustic contrast factors and compressibility between the two cancer cell types (A549 and MDA-MB-231) are found to be 8.2% and 1.2%, respectively. This result suggests that acoustic contrast factor could be a sensitive parameter for mechanophenotyping compared to compressibility. This difference in acoustic contrast factor may arise from the fact that cancer cells are known to be more compressible than normal cells [37] and the invasive cancer cells are stiffer than normal cells [38]. For A549 and MDA-MB-231 cells, even though their cell sizes have some overlap, there is still a 8.2% difference in acoustic contrast factor, suggesting a clear difference in the mechanical properties of these similarly sized cancer cells. We speculate that the smaller acoustic contrast factor of A549 may be related to their higher invasive capacity, as cells require higher compressibility to migrate through the extracellular matrix and move within the original tissue [39,28]. The results demonstrate that the acoustic contrast factor can be used as a useful parameter to distinguish and mechanophenotype these three cell types.

Furthermore, once the acoustic contrast factor is known, the trend of cell movement in the acoustofluidic channel could be determined. From an engineering point of view, the need for tracking cells through image processing is greatly simplified. Our method replaces the trajectory fitting in measuring compressibility (such as Ref. [23,40,41]) by registering the threshold input power when the cells converge to the reference trajectory. Compared with the multi-tilted-angle surface acoustic wave compressibility cytometry [24], our method eliminates the need for fabricating the channel with multiple titled walls and saves the cells from impacting on the channel walls. After establishing the reference trajectory, the threshold of the input power can be used to derive the acoustic contract factor and compressibility. This offers a robust solution for label-free acoustofluidic cytometry eliminating the need of the complex optical system.

As an enhanced acoustofluidic chip, the ETA device offers great versatility and dual capability in both separation [42] and mechanophenotyping different types of cells. This will be valuable for identifying and characterising tumour cells without the need of molecular labelling. Given that the complex biological processes behind these phenotypes

can manifest as changes in cell structure, we also expect mechanical phenotyping can be an important, rapid and unbiased-single-cell analytical tool to advance our understanding of biological processes.

Frequency is one of the key device parameters when determining the design of the ETA device. Given the square of the particle critical size is inversely proportional to the working frequency [43], the working frequency of 19.632 MHz in this work results in a critical size of 4 μm, which is considerably smaller than most of the cell types in the experiment. Further increasing the working frequency to 30–40 MHz allows the ETA device to effectively mechanically phenotype smaller cells, e.g., erythrocytes (4–10 μm) [44] and platelets (1–2 μm) [45]. Submicrometer particles have been successfully manipulated and sorted by using a combined electric and acoustic field [46], which embraces both dielectrophoretic and acoustophoretic forces to lower the critical diameter. The combination overcomes the general problem in sole acoustophoresis including that higher frequency causes larger acoustic attenuation in water [47] and stronger streaming effect [48]. The channel dimensions used in the present work can be further optimised to reduce the cell/microparticle aggregation on the top of the channel caused by the vertical focusing. Though reducing the channel height results in less vertical focusing nodes and acoustic attenuation, it can potentially jam the passing cells and block the entire device. The height of 60 μm is recommended by the simulation [34] and friendly for the cell passage.

Given the ETA device configuration is exquisite in both separation and mechanophenotyping, the future work will integrate acoustic measurement of mechanical properties of cells and acoustic sorting for ultimately constructing a mechanophenotyping-activated cell sorting.

4. Conclusions

In this study, we developed a label-free acoustic flow cytometer for measuring the mechanical property of cells using the ETA device. The input threshold power was determined by observing proximity of measured cells trace to the reference trajectory established by using 10-μm PS microspheres. The acoustic contrast factor and compressibility, which can reflect the compressibility and density of the target cells, is calculated using the threshold power. The accuracy of the measurement is greater than 97.63% in the validation with PS microspheres. The acoustic contrast factors of A549, MDA-MB-231, and leukocytes are 0.106, 0.115, 0.147, respectively. The technique provides the opportunity to transfer molecular specificity into label-free cell characterisation. It is anticipated broad use of the acoustic flow cytometry in both fundamental research and biomedical applications, with immediate utility including high throughput differentiating tumour cell types.

CRediT authorship contribution statement

Hanlin Wang: Conceptualization, Data curation, Formal analysis, Methodology, Validation, Visualization, Writing – original draft. **Joe Boardman:** Data curation, Formal analysis, Methodology. **Xiaoyan Zhang:** Formal analysis, Investigation, Methodology, Project administration, Visualization. **Chao Sun:** Funding acquisition, Writing – review & editing. **Meng Cai:** Resources. **Jun Wei:** Resources. **Zhiqiang Dong:** Resources. **Mingqian Feng:** Resources. **Dongfang Liang:** Writing – review & editing. **Sheng Hu:** Resources. **Yu Qian:** Resources. **Shuang Dong:** Resources. **Yongqing Fu:** Writing – review & editing. **Hamdi Torun:** Methodology. **Aled Clayton:** Writing – review & editing. **Zhenlin Wu:** Writing – review & editing. **Zhihua Xie:** Writing – review & editing. **Xin Yang:** Conceptualization, Funding acquisition, Investigation, Methodology, Project administration, Supervision, Writing – original draft.

Declaration of competing interest

The authors declare that they have no known competing financial interests or personal relationships that could have appeared to influence the work reported in this paper.

Data availability

Data will be made available on request.

Acknowledgements

This work was supported by the Natural Science Basic Research Program of Shaanxi Province (2020JQ-233); the Engineering and Physical Sciences Research Council (EPSRC) (EP/P002803/1 and EP/P018998/1); and the Royal Society (IEC/NSFC/170142, IE161019).

References

[1] P. Augustsson, J.T. Karlsen, H.-W. Su, H. Bruus, J. Voldman, Nat. Commun. 7 (2016), 11556.
[2] H. Mohammadi, E. Sahai, Nat. Cell Biol. 20 (2018) 766–774.
[3] Y.Q. Chen, H.Y. Lan, Y.C. Wu, W.H. Yang, A. Chiou, M.H. Yang, J. Cell Mol. Med. 22 (2018) 3837–3846.
[4] M. Kozminsky, L.L. Sohn, Biomicrofluidics 14 (2020), 031301.
[5] D. Di Carlo, J. Lab. Autom. 17 (2012) 32–42.
[6] M. Urbanska, H.E. Muñoz, J. Shaw Bagnall, O. Otto, S.R. Manalis, D. Di Carlo, J. Guck, Nat. Methods 17 (2020) 587–593.
[7] X. Ding, S.-C.S. Lin, M.I. Lapsley, S. Li, X. Guo, C.Y. Chan, I.K. Chiang, L. Wang, J. P. McCoy, T.J. Huang, Lab Chip 12 (2012) 4228–4231.
[8] S. Li, X. Ding, F. Guo, Y. Chen, M.I. Lapsley, S.-C.S. Lin, L. Wang, J.P. McCoy, C. E. Cameron, T.J. Huang, Anal. Chem. 85 (2013) 5468–5474.
[9] L. Ren, Y. Chen, P. Li, Z. Mao, P.-H. Huang, J. Rufo, F. Guo, L. Wang, J.P. McCoy, S. J. Levine, T.J. Huang, Lab Chip 15 (2015) 3870–3879.
[10] P. Li, Z. Mao, Z. Peng, L. Zhou, Y. Chen, P.-H. Huang, C.I. Truica, J.J. Drabick, W. S. El-Deiry, M. Dao, S. Suresh, T.J. Huang, Proc. Natl. Acad. Sci. U. S. A. 112 (2015) 4970.
[11] M. Wu, Z. Mao, K. Chen, H. Bachman, Y. Chen, J. Rufo, L. Ren, P. Li, L. Wang, T. J. Huang, Adv. Funct. Mater. 27 (2017), 1606039.
[12] P. Sehgal, B.J. Kirby, Anal. Chem. 89 (2017) 12192–12200.
[13] H. Ahmed, G. Destgeer, J. Park, M. Afzal, H.J. Sung, Anal. Chem. 90 (2018) 8546–8552.
[14] J.P. Lata, F. Guo, J. Guo, P.H. Huang, J. Yang, T.J. Huang, Adv. Mater. 28 (2016) 8632–8638.
[15] S. Ciancia, A. Cafarelli, A. Zahoranova, A. Menciassi, L. Ricotti, Front. Bioeng. Biotechnol. 8 (2020) 895–1252.
[16] A. Rajapaksa, A. Qi, L.Y. Yeo, R. Coppel, J.R. Friend, Lab Chip 14 (2014) 1858–1865.
[17] G.K. Chan, S. Wilson, S. Schmidt, J.G. Moffat, J. Lab. Autom. 21 (2016) 125–132.
[18] M. Wu, P.-H. Huang, R. Zhang, Z. Mao, C. Chen, G. Kemeny, P. Li, A.V. Lee, R. Gyanchandani, A.J. Armstrong, M. Dao, S. Suresh, T.J. Huang, Small 14 (2018), 1801131.
[19] S. Li, F. Ma, H. Bachman, C.E. Cameron, X. Zeng, T.J. Huang, J. Micromech. Microeng. 27 (2016), 015031.
[20] S. Li, L. Ren, P.-H. Huang, X. Yao, R.A. Cuento, J.P. McCoy, C.E. Cameron, S. J. Levine, T.J. Huang, Anal. Chem. 88 (2016) 5655–5661.
[21] Z. Wang, F. Li, J. Rufo, C. Chen, S. Yang, L. Li, J. Zhang, J. Cheng, Y. Kim, M. Wu, J. Mol. Diagn. 22 (2020) 50–59.
[22] X. Ding, Z. Peng, S.C. Lin, M. Geri, S. Li, P. Li, Y. Chen, M. Dao, S. Suresh, T. J. Huang, Proc. Natl. Acad. Sci. U. S. A. 111 (2014) 12992–12997.
[23] H. Wang, Z. Liu, D.M. Shin, Z.G. Chen, Y. Cho, Y.-J. Kim, A. Han, Lab Chip 19 (2019) 387–393.
[24] Y. Wu, A.G. Stewart, P.V. Lee, Lab Chip 21 (2021) 2812–2824.
[25] L. Ren, S. Yang, P. Zhang, Z. Qu, Z. Mao, P.H. Huang, Y. Chen, M. Wu, L. Wang, P. Li, Small 14 (2018), 1801996.
[26] L. Zhao, P. Niu, E. Casals, M. Zeng, C. Wu, Y. Yang, S. Sun, Z. Zheng, Z. Wang, Y. Ning, X. Duan, W. Pang, Lab Chip 21 (2021) 660–667.
[27] M. Wu, C. Chen, Z. Wang, H. Bachman, Y. Ouyang, P.-H. Huang, Y. Sadovsky, T. J. Huang, Lab Chip 19 (2019) 1174–1182.
[28] Y. Wu, A.G. Stewart, P.V.S. Lee, Biomicrofluidics 13 (2019), 024107.
[29] R. Barnkob, I. Iranmanesh, M. Wiklund, H. Bruus, Lab Chip 12 (2012) 2337–2344.
[30] K. Olofsson, B. Hammarström, M. Wiklund, Lab Chip 20 (2020) 1981–1990.
[31] M. Wu, A. Ozcelik, J. Rufo, Z. Wang, R. Fang, T. Jun Huang, Microsyst Nanoeng 5 (2019) 32.
[32] T. Frommelt, M. Kostur, M. Wenzel-Schäfer, P. Talkner, P. Hänggi, A. Wixforth, Phys. Rev. Lett. 100 (2008), 034502.
[33] H. Bruus, Lab Chip 11 (2011) 3742–3751.
[34] J. Dong, D. Liang, X. Yang, C. Sun, Ultrasonics 117 (2021), 106547.
[35] S. Kumar Asadullah, N. Saxena, M. Sarkar, A. Barai, S. Sen, J. Cell Sci. (2021) 134.
[36] E. Anderson, D. Petersen, R. Tobey, Biophys. J. 10 (1970) 630–645.
[37] J. Guck, S. Schinkinger, B. Lincoln, F. Wottawah, S. Ebert, M. Romeyke, D. Lenz, H. M. Erickson, R. Ananthakrishnan, D. Mitchell, J. Käs, S. Ulvick, C. Bilby, Biophys. J. 88 (2005) 3689–3698.
[38] J.R. Staunton, B.L. Doss, S. Lindsay, R. Ros, Sci. Rep. 6 (2016), 19686.

[39] T. Yang, F. Bragheri, G. Nava, I. Chiodi, C. Mondello, R. Osellame, K. Berg-Sørensen, I. Cristiani, P. Minzioni, Sci. Rep. 6 (2016), 23946.
[40] Q. Fu, Y. Zhang, T. Huang, Y. Liang, Y. Liu, Biomicrofluidics 15 (2021), 064101.
[41] F. Garofalo, A. Lenshof, A. Urbansky, F. Olm, A.C. Bonestroo, L. Ekblad, S. Scheding, T. Laurell, Microfluid. Nanofluidics 24 (2020) 64.
[42] F. Wu, M.H. Shen, J. Yang, H. Wang, R. Mikhaylov, A. Clayton, X. Qin, C. Sun, Z. Xie, M. Cai, IEEE Electron. Device Lett. 42 (2021) 577–580.
[43] R. Barnkob, P. Augustsson, T. Laurell, H. Bruus, Phys. Rev. 86 (2012), 056307.
[44] M. Kinnunen, A. Kauppila, A. Karmenyan, R. Myllylä, Biomed. Opt Express 2 (2011) 1803–1814.
[45] J. Paulus, Blood 46 (1975) 321–336.
[46] M. Tayebi, D. Yang, D.J. Collins, Y. Ai, Nano Lett. 21 (2021) 6835–6842.
[47] X.M. Tang, M.N. Toksöz, P. Tarif, R.H. Wilkens, J. Acoust. Soc. Am. 83 (1988) 453–462.
[48] K.D. Frampton, S.E. Martin, K. Minor, Appl. Acoust. 64 (2003) 681–692.